DOI: 10.13009/EUCASS2017-30

Numerical exploration on the drag ad heat flux reduction mechanism of blunted cone with aerodisks

Wei Huang, Lang-quan Li*, Li Yan*, Xiao-qian Chen** and Tian-tian Zhang**
**Science and Technology on Scramjet Laboratory, National University of Defense Technology*
Changsha, Hunan 410073, People's Republic of China
***College of Aerospace Science and Engineering, National University of Defense Technology*
Changsha, Hunan 410073, People's Republic of China

Abstract
The flow fields around a blunt cone with and without aerodisk flying at hypersonic Mach numbers are computed numerically by specifying the freestream velocity, static pressure and static temperatures at the inlet of the computational domain with a three-dimensional, steady, Reynolds-averaged Navier-Stokes equation, and an aerodisk is attached to the tip of the rod to reduce the drag and heat flux further. The influences of the length of rod and the diameter of aerodisk on the drag and heat flux reduction mechanism are analyzed comprehensively, and eight configurations are considered in the current study.

1. Introduction

The major challenge among a number of design requirements for hypersonic vehicles is the reduction of drag and aerodynamic heating, and many techniques, for example, concentrated energy deposition along the stagnation streamline [1], a retractable aerospike ahead of the blunt body [2], and a counterflowing jet in the stagnation zone of the blunt body [3] [4] [5] [6], have been proposed to reduce the drag and heat release [7]. Huang gave a survey on the drag and heat release reduction induced by a counterflowing jet and its combinations in 2015, including the combination of the counterflowing jet and a forward-facing cavity [8] [9] [10] [11], the combination of the counterflowing jet and an aerospike [12] [13] [14], and the combination of the counterflowing jet and energy deposition [15]. Of all these techniques of drag and heat flux reduction, application of forward facing aerospike conceived in 1950s is an effective and simpler technique to reduce the drag as well as the heat transfer rate for blunt nosed bodies at hypersonic Mach numbers, and Ahmed and Qin provided a detailed review on the spiked hypersonic vehicle in 2011 [15].

Menezes et al. [16] [17] measured the aerodyanmic drag on a 120-deg apex-angle blunt cone with and without forward-facing aerospikes at various angles of attack at freestream Mach number 5.75 in hypersonic shock tunnel HST2, and a drag reduction of around 55% at zero degree angle of attack was obtained. d'Humières and Stollery [18] tested a spiked body at Mach number 8.2 in a hypersonic wind tunnel, and a maximum drag reduction of 77% of the unspiked body was obtained. Further, Kulkarni et al. [19] studied the influence of a flat-disc-tipped aerospike configuration on drag of a 120 deg apex-angle blunt cone under various total-enthalpy conditions in conventiaonal and free-piston-driven shock tunnels at Mach number 8.0, and a wave drag reduction of about 57% was generated. Kalimuthu et al. [20] [21] conducted an experiment to investigate the effects of the spike length, shape, spike nose configuration and angle of attack on the drag reduction at Mach number 6.0, and the obtained results show that the inclusion of an aerodiak at the tip of the spike is beneficial for the drag reduction if it is at an angle of attack. The same conclusion was obtained by Tahani et al. [22] as well, and 60% and 15% reduction in drag and wall temperature responses were produced respectively. Sebastian et al. [23] studied the influences of length-to-diameter ratio and angle of attack on the drag reduction of a blunted nose cone fitted with an aerospike numerically, and the predicted results agree well with those obtained by Kalimuthu et al. [20]. Mehta [24] [25] evaluated the effect of the various types of aerospike configurations on the drag reduction numerically at a length-to-diameter ratio of 0.5, at Mach number 6.0 and at a zero angle of attack. Gerdroodbary and Hosseinalipour [26] studied the influence of the aerospike on the surrounding flowfield of a large-angle blunt cone for freestream Mach number of 5.75, and additional modifications to the tip of the spike were taken into consideration as well, including a cut spike, and a flat and hemispherical aerodisk mounted on the tip of the spike. The impact of the aerodisk on the aeroheating reduction capabilities of the spiked blunt bodies at Mach 6.0 flight conditions was evaluated numerically

Copyright © 2017 by Wei Huang, Lang-quan Li, Li Yan, Xiao-qian Chen and Tian-tian Zhang.
Published by the EUCASS association with permission.

DOI: 10.13009/EUCASS2017-30

by Ahmed and Qin [27] [28], and adding an aerodisk can degrade the performance of the spike in heat flux reduction. Yadav and Guven [29] investigated the turbulent reattachment heat flux of a generic blunt body with doule-disk aerospike at freestream Mach number 6.2 numerically, and the predicted results were compared with those of the same blunt body without aerospike. The proposed strategy shows favourable reattachment heat flux reduction, as well as drag reduction of the main body. Different Mach numbers at different altitudes were chosen by Gauer and Paull [30] to investigate the effect of the aerospike on the surrounding flowfield of a nose cone, and some additional modifications to the tip of the spike were considered as well, including a sharp front, a blunt spike, and an aerodome mounted on the tip of the spike. A blunt body, a classical disk-tip spike, a sphere-tip spike, and a biconical-tip spike were studied by Gnemmi et al. [31] experimentally and numerically for a large range of attack angles at a Mach number of 4.5. In 2016, the fluid-thermal interaction between the external flowfield and the internal structure of a spiked blunt body at freestream Mach numebr 5.0 was investigated numerically by Guo et al. [32], and the coupled fluid-thermal analysis is very crucial for the aerothermal environment prediction of the spiked blunt body.
From the literature mentioned above, it is clearly seen that the mechanical spike is an effective way to reduce the aerodynamic drag due to the reduced dynamic pressure in the separated flow region, and adding a disk on the spike nose can yield better performance for thermal protection and drag reduction compared with the pointed spike. Further, The flow field around a spiked blunt body appears to be very complex and contains a number of interesting flow phenomena and characteristics, which are yet to be investigated. Thus, in this paper, the drag and heat flux reduction mechanism induced by the aerodisk has been investigate numerically, and eight configurations have been taken into consideration, as well as two turbulence models, namely the SST k-ω and S-A models. The spiked blunt body without the aerodisk has been set to be the base model.

2. Physical model and numerical approach

2.1 Physical model

The geometry considered in this work is an axisymmetric hemisphere-cylinder forebody with a spike, a thin cylindrical rod, attached at the stagnation point, and an aerodisk is attached to the tip of the rod, see Fig.1. The dimensions of the blunt body with the aerodisk are illustrated in Fig.1 as well. The diameter of the cylinder is 80mm, and the length of the hemisphere-cylinder forebody is 200mm. The length of the spike and the diameter of the aerodisk are both variable in order to evaluate their influences on the drag and heat flux reduction of the blunt body. In the current study, the length of the spike is set to be 40mm, 65mm and 80mm, and the diameter of the aerodisk is set to be 10mm, 14mm and 18mm, see Table.1. The spiked blunt body without the aerodisk is set to be the base model, namely A0, and Fig.2 shows the three-dimensional view of the blunt cone with the aerodisk (A3).

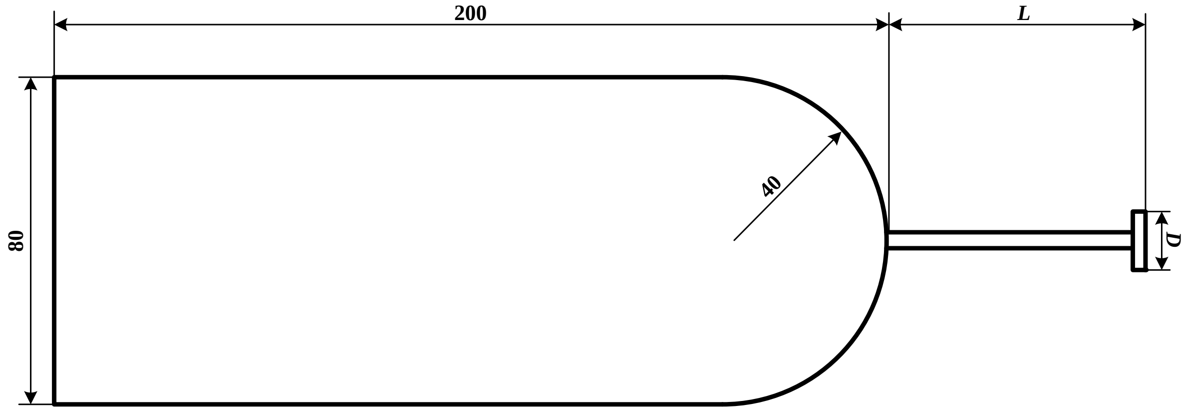

Figure 1: Schematic diagram of the blunt cone with aerodisk (unit: mm)

Table 1: Test cases

Parameter	A0	A1	A2	A3	B1	B2	B3	C3
L(mm)	40	40	40	40	65	65	65	80
D(mm)	0	10	14	18	10	14	18	18

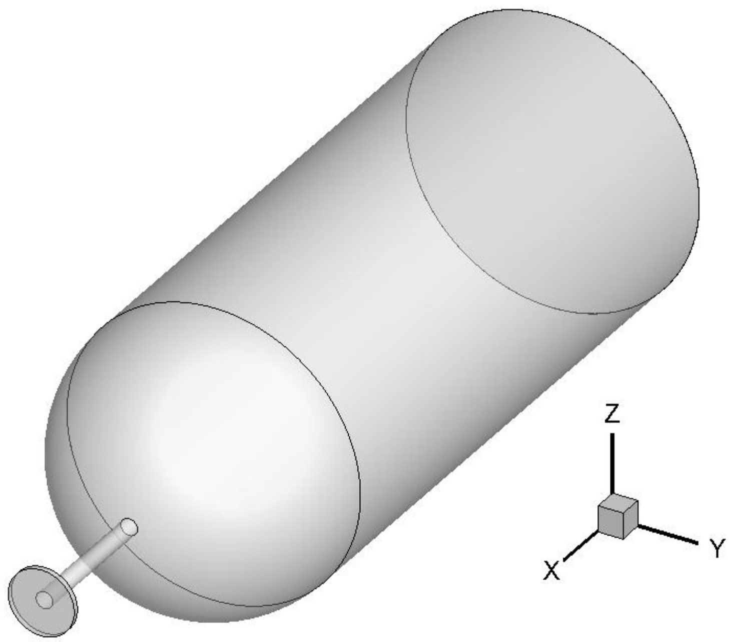

Figure 2: 3-D view of the blunt cone with the aerodisk (A3)

The freestream conditions are chosen as zero angles of attack, P_∞=1000kPa, T_∞=373K and Ma=4.937. The Reynolds number Re, based on the main body diameter and freestream conditions, equals 2.2×10^7 in the current study, which means that turbulent effects should be considered according to Crawford's results [33]. Therefore, a fully turbulent flow condition is assumed in the present study.

2.2 Numerical approach

The steady state computational data have been obtained using FLUENT version 6.3.26, and the mesh generation has used the commercial software Gambit [34]. A Dell workstation at Science and Technology on Scramjet Laboratory, using up to 32 processors, has provided a parallel computing environment for flow solutions.

For this study, the three-dimensional Reynolds-average Navier-Stokes (RANS) equations have been solved using a coupled, implicit, second-order upwind solver, and it is a steady-state model. Cell fluxes have been computed using an AUSM scheme, and the viscosity has been determined using mass-weighted-mixing-law. The operational fluid is air, and it is treated as an ideal gas with no reactions modeled.

The turbulent viscosity is calculated by two equation *k*-*ω* shear stress transport (SST) turbulence model, and the Spalart-Allmaras model is employed to investigate the influence of the turbulence model on the predicted results, such as the static pressure distribution. The SST model combines the advantages of the *k*-*ω* model near solid surfaces with the *k*-*ε* model, which owns good free-shear-flow properties, making it well suited for this flow. The SST model also owns improved performance in adverse pressure gradient flows over either the *k*-*ω* or *k*-*ε* models [35], and the transport equations for *k* and *ω* can refer to Ref. [36], see the equations.(1) and (2). The SST model was utilized successfully in previous studies on transverse injection flow [37] [38] [39]. The Courant-Friedrichs-Levy (CFL) number defines the progress in grid cells of the considered size for one time step, and it remains at 0.5 with suitable under-relaxation factors to ensure stability.

$$\frac{\partial}{\partial \mathrm{t}}(\rho k)+\frac{\partial}{\partial x_i}(\rho k u_i)=\frac{\partial}{\partial x_j}\left(\Gamma_k\frac{\partial k}{\partial x_j}\right)+\widetilde{G_k}-Y_k+S_k \tag{1}$$

$$\frac{\partial}{\partial \mathrm{t}}(\rho\omega)+\frac{\partial}{\partial x_i}(\rho\omega u_i)=\frac{\partial}{\partial x_j}\left(\Gamma_\omega\frac{\partial\omega}{\partial x_j}\right)+G_\omega-Y_\omega+D_\omega+S_\omega \tag{2}$$

The compressibility takes part in dissipation terms such as Y_k and Y_ω and partically in the production of turbulence kinetic energy is defined as follows:

$$Y_k=\rho\beta^*k\omega \tag{3}$$

$$Y_\omega=\rho\beta\omega^2 \tag{4}$$

Herein, β^* and β are functions of $F(M_t)$.

$$\beta^*=\beta_i^*[1+\zeta^*F(M_t)] \tag{5}$$

$$\beta=\beta_i\left[1-\frac{\beta_i^*}{\beta_i}\zeta^*F(M_t)\right] \tag{6}$$

DOI: 10.13009/EUCASS2017-30

ζ^* = 1.5, and the compressibility function $F(M_t)$ is defines as follows:

$$\mathrm{F}(M_t)=\begin{cases} 0 & M_t \le M_{t0} \\ M_t^2 - M_{t0}^2 & M_t > M_{t0} \end{cases} \tag{7}$$

Where,

$$M_t^2 = \frac{2k}{\alpha^2} \tag{8}$$

$$M_{t0} = 0.25 \tag{9}$$

$$\alpha = \sqrt{\gamma RT} \tag{10}$$

The term $\widetilde{G_k}$ represents the production of turbulence kinetic energy, and it is affected by compressibility as well. The equation of $\widetilde{G_k}$ is defined as follows:

$$\widetilde{G_k} = \min(G_k, 10\rho\beta^* k\omega) \tag{11}$$

The flow fields around the blunt cone with and without aerospike flying at hypersonic Mach numbers are computed numerically by specifying the freestream velocity, static pressure and static temperatures at the inlet of the computational domain. The no-slip conditions (u = v = w = 0.0) are assumed for wall boundaries, and a constant temperature of 300K is specified at the walls.. At the outlet of the computational domain, all variables are extrapolated from the interior domain, that is, a supersonic outlet is employed at the nodes of the outlet region [40]. A faster convergence can be achieved, and thus a shorter computation time, when the initial conditions are chosen as close as possible to the final steady-state values [41]. However, the highly complicated flowfield, which is characterized by several different flow zones, makes it impossible to adapt the initial conditions close to the steady-state values. Therefore, the initial conditions are defined to be equal to the freestream values.

The quality of the mesh plays a significant role in the accuracy and stability of the numerical computation, and one of the controlling factors for the numerical simulation is the proper grid arrangement. The grid density is clustered towards the walls for all grids, see Fig.3, and the total number of the grid cells is about 2.5 million for all cases studied. Fig.3 shows the grid system in the symmetric plane of the blunt cone with aerodisk (A3). A boundary layer grid is generated on the walls with a first cell height of 0.01mm, which results in a suitable value of y^+ for all of the flow fields, namely its maximum value is less than 10.0.

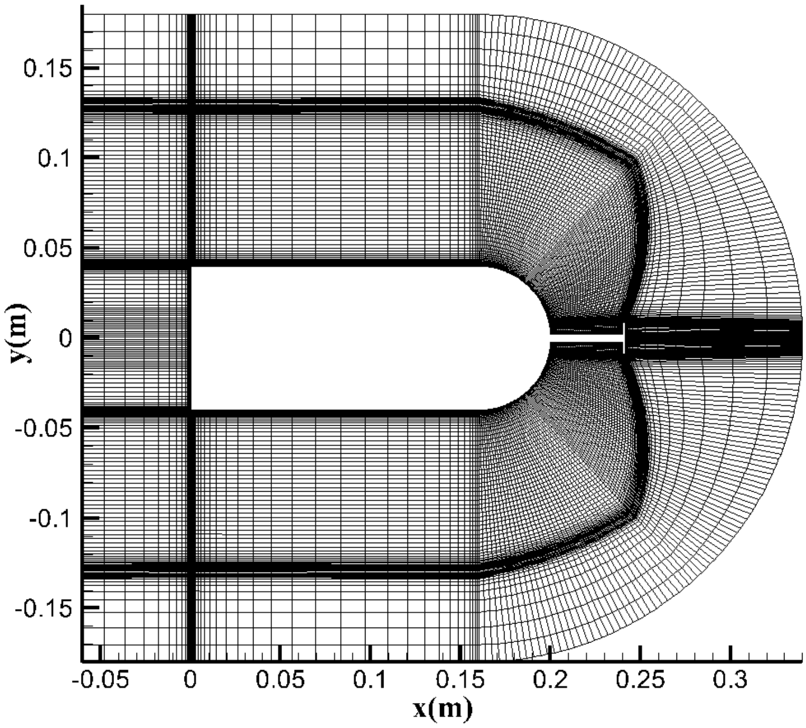

Figure 3: Grid system in the symmetric plane of the blunt cone with aerodisk (A3)

3. Results and discussion

Fig.4 shows the comparison of static pressure distributions along the blunt cone, and the predicted results are obained by the SST k-ω and S-A models. In Fig.4, it is clearly observed that the static pressure distribution obtained by the SST k-ω turbulence model meets suitably with that obained by the S-A model, and some discrepancies may be induced by the unsteady oscillation of the specified configuration. Therefore, the predicted results obtained by the

SST k-ω turbulence model are with confidence in the following discussion. The surface static pressure on the blunt body can be substantially reduced if an aerodisk is attached to the tip of the rod, and the aerodisk geometry drastically influences the aerodynamic drag of the blunted body at high speeds. Thus, the introduction of the aerodisk decreases the aerodynamic drag force. The aerodynamic drag force (F) included the pressure drag force (F_P) and the viscous drag force (F_v), and the maximum reduction of the pressure drag force is about 55.46%, see Table.2. However, the maximum reduction of the viscous drag force is only about 27.48%. In Table.2, we can observe that the maximum aerodynamic drag reduction occurs in the model C3 with the longest spike and the largest diamter of the aerodisk irrespective of the pressure drag force and the viscous drag force, and the reduction in drag of the blunt body is proportional to the length of the spike and the diameter of the aerodisk. The maximum aerodynamic drag reduction is 54.92%, see Table.2. Table.2 represents the aerodynamic drag comparision for the blunt cone with different aerodisks, and Δ is the drag reduction coefficient. Δ is defined as

$$\Delta = \frac{F_{ref} - F}{F_{ref}} \times 100\% \tag{12}$$

Herein, F is the drag force for each case studied, and F_{ref} is the drag force of the spiked blunt body without the aerodisk, namely A0.

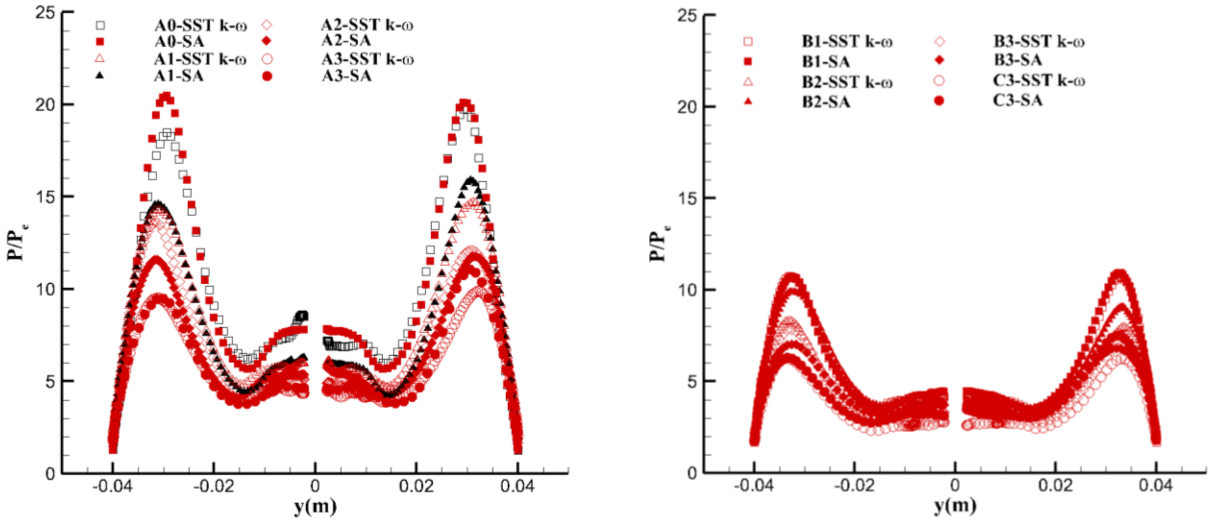

Figure 4: Comparison of static pressure distributions along the blunt cone

Table 2: Aerodynamic drag comparison for the blunt cone with different aerodisks

Parameter	A0	A1	A2	A3	B1	B2	B3	C3
F_p(N)	113.09	97.15	86.99	77.05	69.77	59.54	57.98	50.37
F_v(N)	2.22	2.05	1.98	1.82	1.90	1.76	1.71	1.61
F(N)	115.31	99.20	88.97	78.87	71.67	61.30	59.69	51.98
Δ	0	-13.97%	-22.84%	-31.60%	-37.85%	-46.84%	-48.24%	-54.92%

Fig.5 shows the density contour comparison for the blunt cone with different aerodisks, and the predicted results are obtained by the SST k-ω turbulence model. It is obvious that a conical shock wave is generated by attaching a forward-facing aerodisk, and the maximum value of the density distribution decreases with the increase of the diameter of the aerodisk, see Figs.5(b), (c) and (d), as well as the increase of the length of the spike, see Figs.5(b) and (e). Because of the reattachment of the shear layer on the shoulder of the blunt body, the pressure near that point becomes large, and this conclusion is consistent with the static pressure distribution along the blunt cone, see Fig.4. At the same time, the location of the peak value moves slightly downstream with the increase of the diameter of the aerodisk, as well as the length of the spike.

DOI: 10.13009/EUCASS2017-30

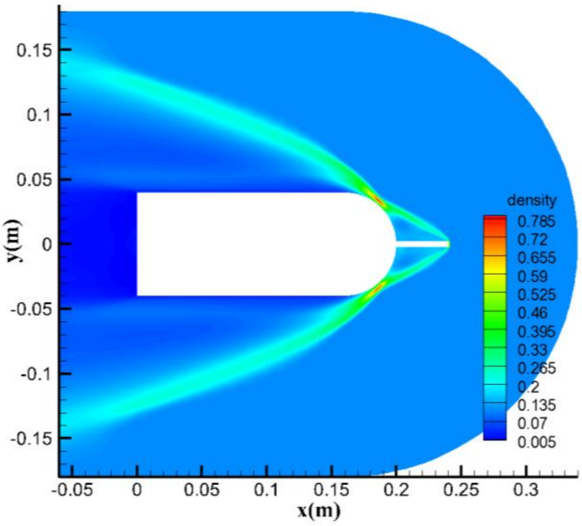

(a) A0

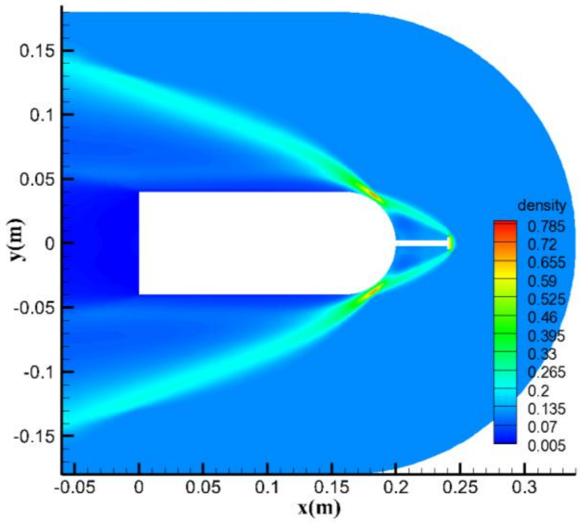

(b) A1

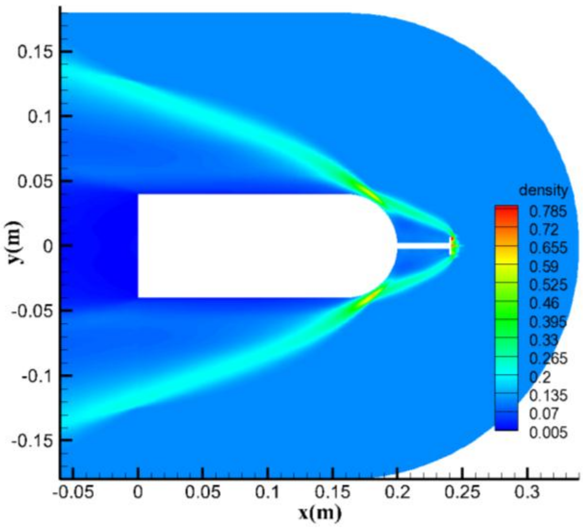

(c) A2

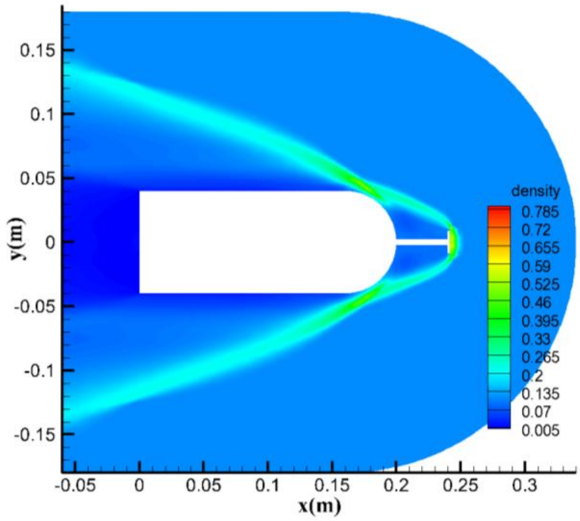

(d) A3

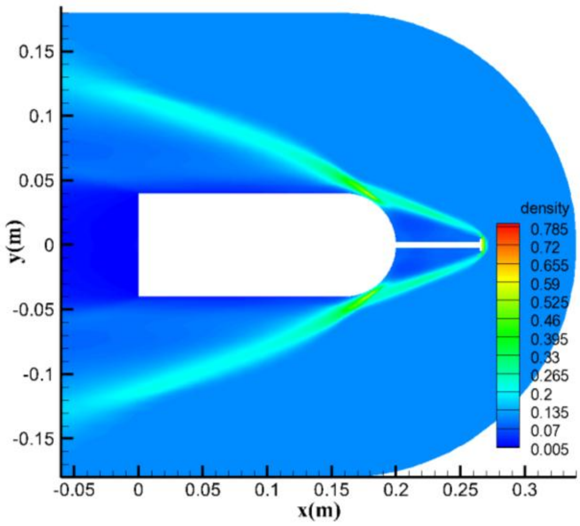

(e) B1

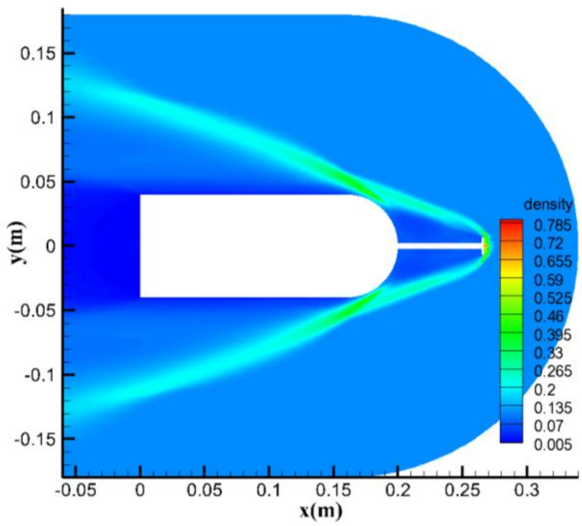

(f) B2

DOI: 10.13009/EUCASS2017-30

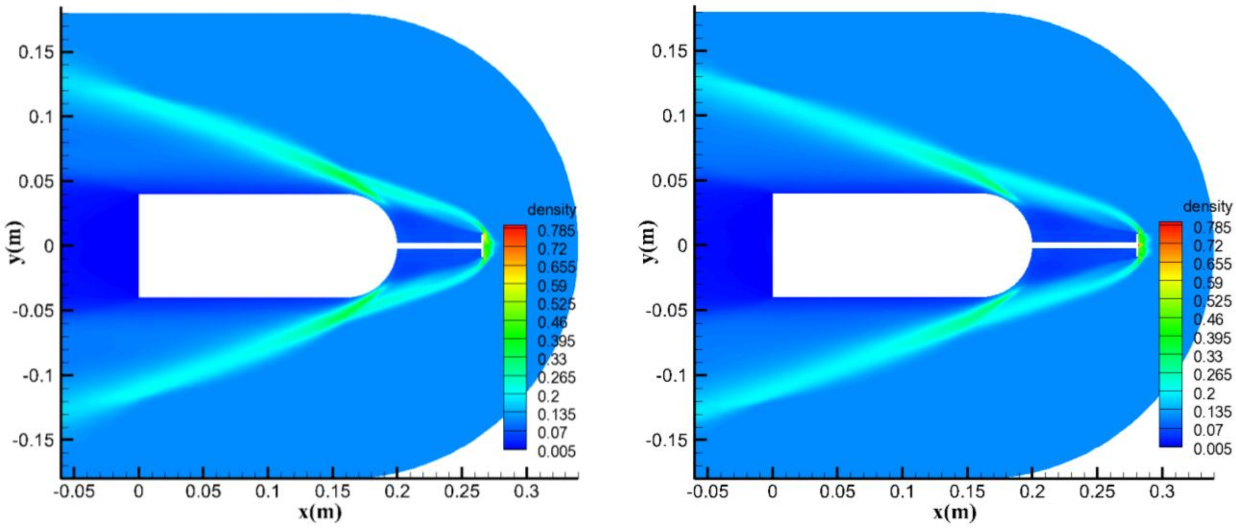

(g) B3 (h) C3

Figure 5: Density contour comparison for the blunt cone with different aerodisks, and the predicted results are obtained by the SST k-ω turbulence model

Fig.6 shows the comparison of static temperature curve for the blunt cone with different aerodisks, and the predicted results are obtained by the SST k-ω turbulence model. It is shown that the variable range of the static temperature along the blunt cone is 300-400K, and the length of the spike and the diameter of the aerodisk both have a slight impact on the static temperature distribution. Due to the unsteady oscillation induced by the specified configuration, the static temperature distribution oscillates in the vicinity of the spike root, and the unsteady simulation will be conducted in the near future.

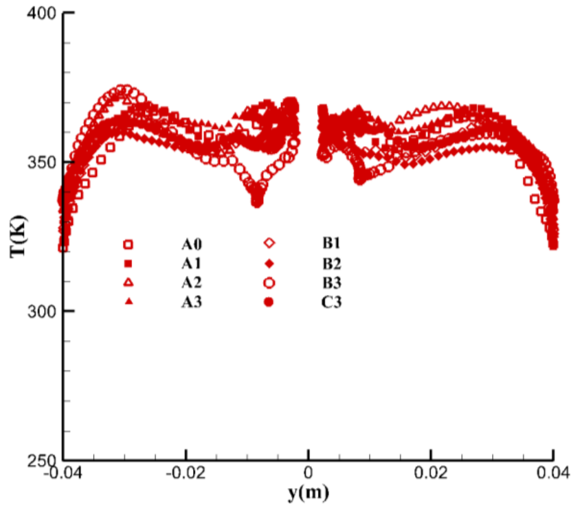

Figure 6: Comparison of static temperature curve for the blunt cone with different aerodisks, and the predicted results are obtained by the SST k-ω turbulence model

Fig.7 shows the static temperature contour and streamline comparison for the blunt cone with different aerodisks, and the predicted results are obtained by the SST k-ω turbulence model. It is clearly shown that the spike produces a region of recirculating separated flow that shields the blunt-nosed body from the incoming flow, and the recirculating region is formed around the root of the spike up to the reattachment point of the flow at the shoulder of the blunt body. The size of the recirculating region increases with the increase of the diameter of the aerodisk, especially with the increase of the length of the spike, see Figs.7(e), (f), (g) and (h). The length of the spike and diameter of the aerodisk both have an especially great influence on the shape of the recirculation area, and they have to be suitably chosen to obtain a large conical recirculation area in front of the blunt body to obtain maximum drag reduction. The aerodynamic drag reduction of the blunt body is proportional to the extent of the recirculating dead air region. The dynamic pressure in the recirculation area is highly reduced and thus leads to the decrease in drag force on the surface of the blunt body.

DOI: 10.13009/EUCASS2017-30

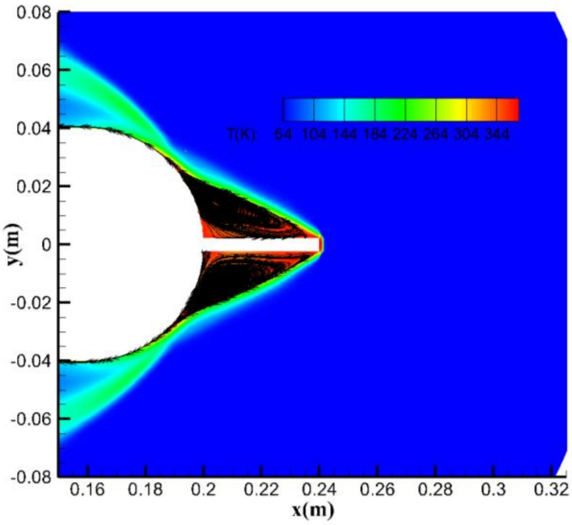

(a) A0

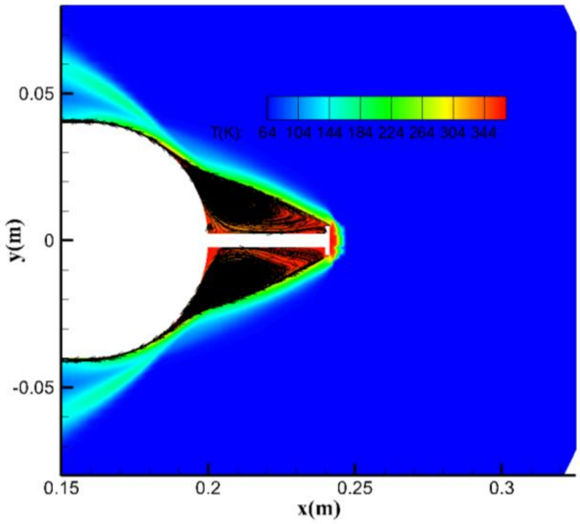

(b) A1

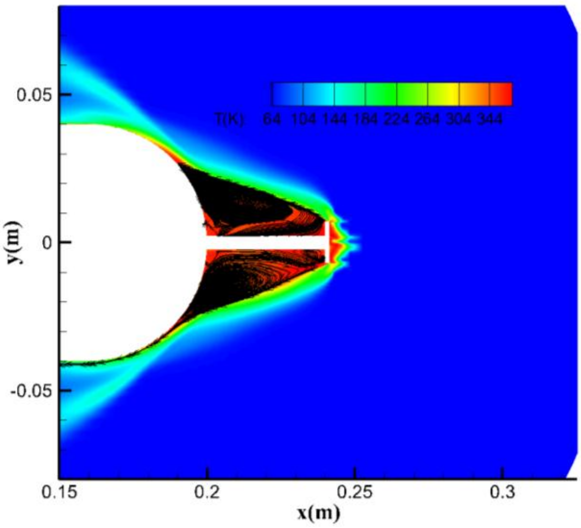

(c) A2

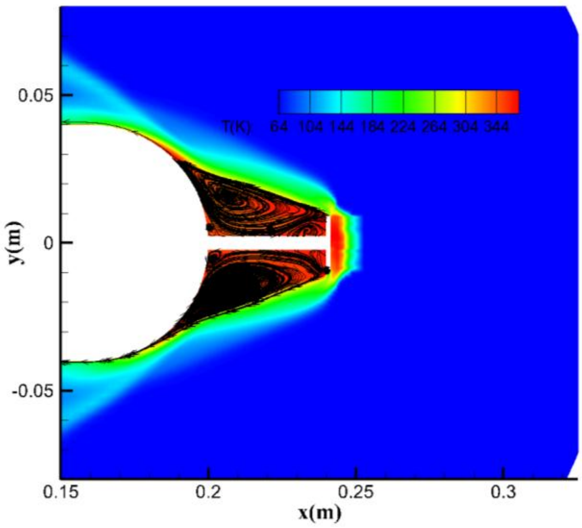

(d) A3

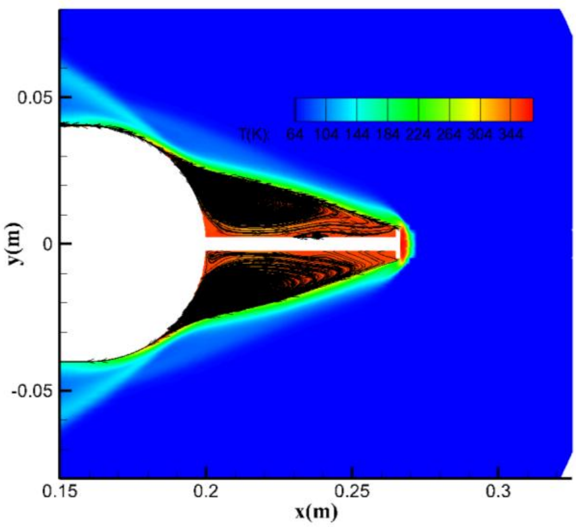

(e) B1

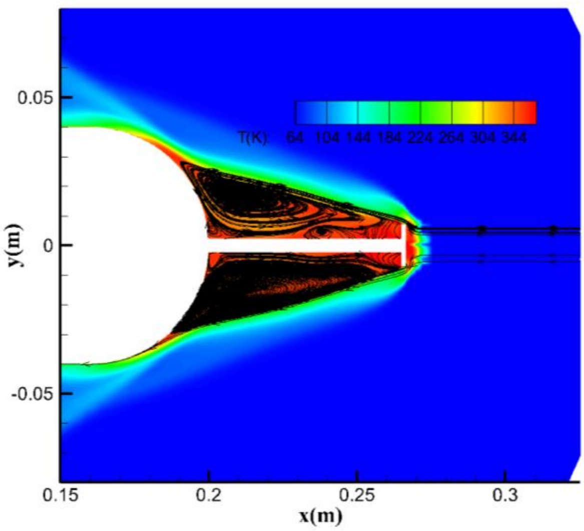

(f) B2

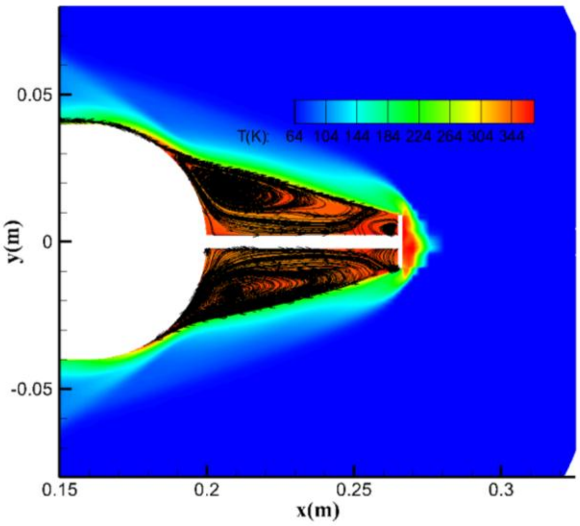

(g) B3

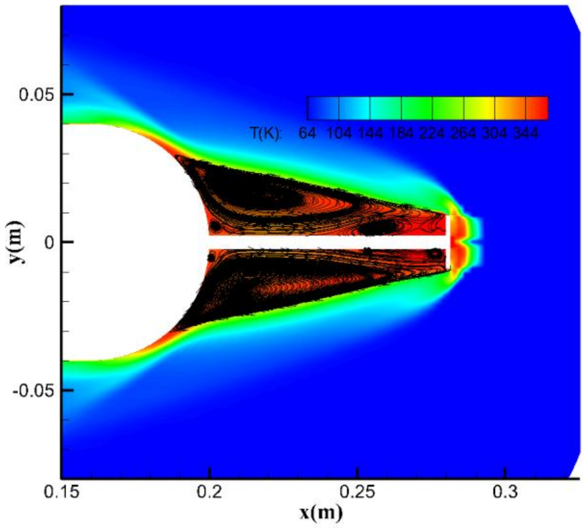

(h) C3

Figure 7: Static temperature contour and streamline comparison for the blunt cone with different aerodisks, and the predicted results are obtained by the SST k-ω turbulence model

4. Conclusion

In the current study, the three-dimensional Reynolds-average Navier-Stokes (RANS) equations coupled with the SST k-ω turbulence model have been employed to investigated the drag and heat flux reduction mechanism in the spiked blunt body with the aerodisk, and the predicted results obtained by the S-A model have used to evaluate the influence of the turbulence model. Eight configurations have been taken into consideration, and the spiked blunt body without the aerodisk has been set to be the base model. We have come to the following conclusions:

- The predicted static pressure distributions for all blunt bodies obtained by the SST k-ω turbulence model agree suitably with those obtained by the S-A model, and some discrepancies may be induced by the unsteady oscillation of the specified configurations.
- The reduction in drag of the blunt body is proportional to the length of the spike and the diameter of the aerodisk, and the maximum aerodynamic drag reduction is 54.92% in the range considered in the current study.
- The variable range of the static temperature along the blunt cone is 300-400K, and the length of the spike and the diameter of the aerodisk both have a slight impact on the static temperature distribution.

Acknowledgements

The authors would like to express their thanks for the support from the National Natural Science Foundation of China (No. 11502291) and the Science Foundation of National University of Defense Technology (No. JC14-01-01).

References

[1] Knight D. 2008. Survey of aerodynamic drag reduction at high speed by energy deposition. *Journal of Propulsion and Power*. 24(6): 1153-1167.
[2] Ahmed M. Y. M., Qin N. 2011. Recent advances in the aerothermodynamics of spiked hypersonic vehicles. *Progress in Aerospace Sciences*. 47: 425-449.
[3] Li S. B., Wang Z. G., Huang W., Liu J. 2016. Effect of the injector configuration for opposing jet on the drag and heat reduction. *Aerospace Science and Technology*. 51: 78-86.
[4] Li S. B., Wang Z. G., Huang W., Liu J. 2017. Drag and heat reduction performance for an equal polygon opposing jet. *Journal of Aerospace Engineering*. 30(1): 04016065.
[5] Li S. B., Wang Z. G., Huang W., Yan L. 2017. Analysis of flowfield characteristics for equal polygon oppsing jet on different freeflow conditions. *Acta Astronautica*. 133: 50-62.
[6] Li S. B., Wang Z. G., Barakos G. N., Huang W., Steijl R. 2016. Research on the drag reduction performance induced by the counterflowing jet for waverider with variable blunt radii. *Acta Astronautica*. 127: 120-130.

[7] Wang Z. G., Sun X. W., Huang W., Li S. B., Yan L. 2016. Experimental investigation on drag and heat flux reduction in supersonic/hypersonic flows: A survey. *Acta Astronautica*. 129: 95-110.
[8] Huang W., Yan L., Liu J., Jin L., Tan J. G. 2015. Drag and heat reduction mechanism in the combinational opposing jet and acoustic cavity concept for hypersonic vehicles. *Aerospace Science and Technology*. 42: 407-414.
[9] Huang W., Jiang Y. P., Yan L., Liu J. 2016. Heat flux reduction mechanism induced by a combinational opposing jet and cavity concept in supersonic flows. *Acta Astronautica*. 121: 164-171.
[10] Sun X. W., Guo Z. Y., Huang W., Li S. B., Yan L. 2016. Drag and heat reduction mechanism induced by a combinational novel cavity and counterflowing jet concept in hypersonic flows. *Acta Astronautica*. 126: 109-119.
[11] Sun X. W., Guo Z. Y., Huang W., Li S. B., Yan L. 2017. A study of performance parameters on drag and heat flux reduction efficiency of combinational novel cavity and opposing jet concept in hypersonic flows. *Acta Astronautica*. 131: 204-225.
[12] Gerdroodbary M. B. 2014. Numerical analysis on cooling performance of counterflowing jet over aerodisked blunt body. *Shock Waves*. 24: 537-543.
[13] Huang W., Liu J., Xia Z. X. 2015. Drag reduction mechanism induced by a combinational opposing jet and spike concept in supersonic flows. *Acta Astronautica*. 115: 24-31.
[14] Eghlima Z., Mansour K. 2017. Drag reduction for the combination of spike and counterflow jet on blunt body at high Mach number flow. *Acta Astronautica*. 133: 103-110.
[15] Huang W. 2015. A survey of drag and heat reduction in supersonic flows by a counterflowing jet and its combinations. *Journal of Zhejiang University – Science A (Applied Physics & Engineering)*. 16(7): 551-561.
[16] Menezes V., Saravanan S., Jagadeesh G., Reddy K. P. J. 2003. Experimental investigations of hypersonic flow over highly blunted cones with aerospikes. *AIAA Journal*. 41(10): 1955-1966.
[17] Menezes V., Saravanan S., Reddy K. P. J. 2002. Shock tunnel study of spiked aerodynamic bodies flying at hypersonic Mach numbers. *Shock Waves*. 12: 197-204.
[18] d'Humières G., Stollery J. L. 2010. Drag reduction on a spiked body at hypersonic speed. *The Aeronautical Journal*. 114(1152): 113-119.
[19] Kulkarni V., Menezes V., Reddy K. P. J. 2010. Effectiveness of aerospike for drag reduction on a blunt cone in hypersonic flow. *Journal of Spacecraft and Rockets*. 47(3): 542-544.
[20] Kalimuthu R., Mehta R. C., Rathakrishnan E. 2008. Experimental investigation on spiked body in hypersonic flow. *The Aeronautical Journal*. 112(1136): 593-598.
[21] Kalimuthu R., Mehta R. C., Rathakrishnan E. 2013. Pressure measurements over a hemisphere-cylinder body attached with a forward facing spike. *Aeronautical Journal*. 117(1192): 639-646.
[22] Tahani M., Karimi M. S., Motlagh A. M., Mirmahdian S. 2013. Numerical investigation of drag and heat reduction in hypersonic spiked blunt bodies. *Heat Mass Transfer*. 49: 1369-1384.
[23] Sebastian J. J., Suryan A., Kim H. D. 2016. Numerical analysis of hypersonic flow past blunt bodies with aerospikes. *Journal of Spacecraft and Rockets*. 53(4): 669-677.
[24] Mehta R. C. 2013. Numerical heat transfer study around a spiked blunt-nose body at Mach 6. *Heat Mass Transfer*. 49: 485-496
[25] Mehta R. C. 2010. Numerical simulation of the flow field over conical, disc and flat spiked body at Mach 6. *The Aeronautical Journal*. 114(1154): 225-236.
[26] Gerdroodbary M. B., Hosseinalipour S. M. 2010. Numerical simulation of hypersonic flow over highly blunted cones with spike. *Acta Astronautica*. 67: 180-193.
[27] Ahmed M. Y. M., Qin N. 2011. Numerical investigation of aeroheating characteristics of spiked blunt bodies at Mach six flight conditions. *The Aeronautical Journal*. 115(1168): 377-386.
[28] Ahmed M. Y. M., Qin N. 2010. Mathmodels for aerothermodynamic design optimization of hypersonic spiked blunt bodies. *Aerospace Science and Technology*. 14: 364-376.
[29] Yadav R., Guven U. 2013. Aerothermodynamics of a hypersonic projectile with a double-disk aerospike. *Aeronautical Journal*. 117(1195): 913-928.
[30] Gauer M., Paull A. 2008. Numerical investigation of a spiked blunt nose cone at hypersonic speeds. *Journal of Spacecraft and Rockets*. 45(3): 459-471.
[31] Gnemmi P., Srulijes J., Roussel K. 2003. Flowfield around spike-tipped bodies for high attack angles at Mach 4.5. *Journal of Spacecraft and Rockets*. 40(5): 622-631.
[32] Guo S., Xu J., Qin Q., Gu R. 2016. Fluid-thermal interaction investigation of spiked blunt bodies at hypersonic flight condition. *Journal of Spacecraft and Rockets*. 53(4): 629-643.
[33] Crawford D. H. 1959. Investigation of the flow over a spiked-nose hemisphere cylinder at a Mach number of 6.8. NASA TN-D-118.
[34] Fluent Inc. 2006. Fluent 6.3 user's guide. Lebanon, NH: Fluent Inc.

[35] Freeborn A. B., King P. I., Gruber M. R. 2009. Swept-leading-edge pylon effects on a scramjet pylon-cavity flameholder flowfield. *Journal of Propulsion and Power*. 25(3): 571-582.
[36] Erdem E., Kontis K. 2010. Numerical and experimental investigation of transverse injection flows. *Shock Waves*. 20: 103-118.
[37] Huang W. 2014. Design exploration of three-dimensional transverse jet in a supersonic crossflow based on data mining and multi-objective design optimization approaches. *International Journal of Hydrogen Energy*. 39: 3914-3925.
[38] Huang W., Liu W. D., Li S. B., Xia Z. X., Liu J., Wang Z. G. 2012. Influences of the turbulence model and the slot width on the transverse slot injection flow field in supersonic flows. *Acta Astronautica*. 73: 1-9.
[39] Huang W. 2015. Effect of jet-to-crossflow pressure ratio arrangement on turbulent mixing in a flowpath with square staged injectors. *Fuel*. 144: 164-170.
[40] Kim K. M., Baek S. W., Han C. Y. 2004. Numerical study on supersonic combustion with cavity-based fuel injection. *International Journal of Heat and Mass Transfer*. 47: 271-286.
[41] Huang W., Li S. B., Yan L., Wang Z. G. 2013. Performance evaluation and parametric analysis on cantilevered ramp injector in supersonic flows. *Acta Astronautica*. 84: 141-152.